

# Hyperparametric Oscillation via Bound States in the Continuum

Fuchuan Lei, Zhichao Ye, Krishna Twayana, Yan Gao, Marcello Girardi, Óskar B. Helgason, Ping Zhao, and Victor Torres-Company\*

*Department of Microtechnology and Nanoscience,  
Chalmers University of Technology SE-41296 Gothenburg, Sweden*

(Dated: February 24, 2023)

Optical hyperparametric oscillation based on the third-order nonlinearity is one of the most significant mechanisms to generate coherent electromagnetic radiation and produce quantum states of light. Advances in dispersion-engineered high- $Q$  microresonators allow for generating signal waves far from the pump and decrease the oscillation power threshold to submilliwatt levels. However, the pump-to-signal conversion efficiency and absolute signal power are low, fundamentally limited by parasitic mode competition and attainable cavity intrinsic  $Q$  to coupling  $Q$  ratio, i.e.,  $Q_i/Q_c$ . Here, we use Friedrich-Wintgen bound states in the continuum (BICs) to overcome the physical challenges in an integrated microresonator-waveguide system. As a result, on-chip coherent hyperparametric oscillation is generated in BICs with unprecedented conversion efficiency and absolute signal power. This work not only opens a path to generate high-power and efficient continuous-wave electromagnetic radiation in Kerr nonlinear media but also enhances the understanding of microresonator-waveguide system - an elementary unit of modern photonics.

Optical hyperparametric oscillation (H-OPO) emerges in a driven  $\chi^{(3)}$  nonlinear cavity as a result of modulation instability (MI) that amplifies vacuum photons. Two pump photons are converted into a pair of correlated photon pairs ( $2\hbar\omega_p \rightarrow \hbar\omega_s + \hbar\omega_i$ ) at new frequencies (Fig. 1(a)). This elementary mechanism lies at the onset of microresonator frequency comb generation [1] and has served for generating coherent light sources [2–7] and quantum technologies [8–14]. High- $Q$  microresonators, either in whispering gallery mode [15, 16], planar [17–24] or photonic crystal cavities [25], provide means to decrease the power oscillation threshold. With dispersion engineering, broadband H-OPO has been demonstrated [26–30].

A critical metric in any parametric oscillator is the conversion efficiency, i.e., the ratio of signal power compared to the pump. This metric is first limited by mode competition among different longitudinal modes in the cavity and nondegenerate four-wave mixing [31]. The gain required to sustain H-OPO originates from MI. For a fixed dispersion, the gain's peak and bandwidth are determined by the pump power [32, 33]. With high pump power, the gain can span multiple free spectral ranges (FSRs), even for extremely small cavities [34, 35], as schematically illustrated in Fig. 1(b). Hence, multiple cavity modes could emit simultaneously once their losses are compensated by the gain. The newly generated frequency components could induce by themselves parametric oscillation, and degrade the coherence through nondegenerate four-wave mixing [34]. To avoid these detrimental effects, one could engineer the resonator's dispersion and pump it with moderate power [26–30, 36]. Another strategy is to reduce the number of effective cavity modes, such as increasing the FSR of microresonators [28, 31] or suppressing undesired modes with the aid of frequency selection elements (see Fig. 1(b)), e.g.,

coupled cavities and gratings [37, 38]. These classical techniques, being widely used for single-frequency lasers, however, cannot be directly adapted for nonlinear optics because they are usually incompatible with the stringent demand of simultaneously attaining high- $Q$ , low-mode volume and dispersion engineering. In addition to multi-mode interaction, the second limiting factor of the conversion efficiency is the attainable  $Q_i/Q_c$  [26], where  $Q_{i(c)}$  is the cavity intrinsic (coupling) quality factor. Realistic microresonator-coupler systems introduce a physical limit because the coupling rate ( $\sim 1/Q_c$ ) cannot be arbitrarily high without involving additional intrinsic loss,

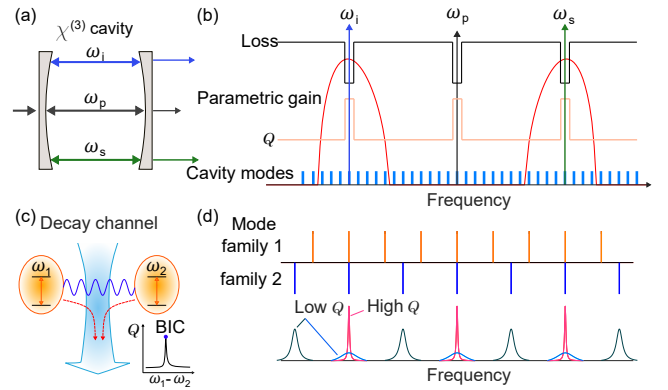


FIG. 1. Concept of H-OPO via bound states in the continuum (BICs). (a) Schematic of H-OPO. (b) Cavity quality factor ( $Q$ ) management for achieving high-efficiency H-OPO. (c) Schematic illustration of the Friedrich-Wintgen BIC. Two near degenerate resonances can be dissipatively coupled if both share a common decay channel. As a result, two supermodes are formed: one is a nondecaying bound state (high  $Q$ ) while the other one is an increased-decaying state (low  $Q$ ). (d) Realization of ( $Q$ ) engineering for cavity modes by making use of BICs in a two-mode cavity, where the high- $Q$  mode can be achieved periodically owing to the Vernier effect.

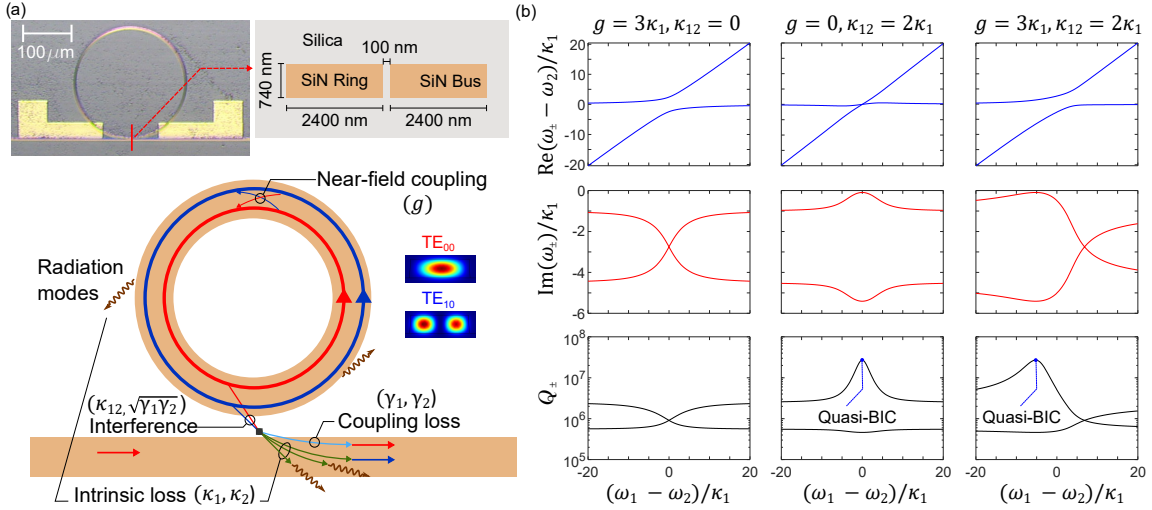


FIG. 2. BICs in a multimode microring-waveguide system. (a) Image and schematic of the system. (b) Calculated eigenfrequencies of  $\mathcal{H}$  and the corresponding  $Q$  as a function of the detuning. Parameters used here:  $\gamma_1 = \gamma_2 = 0$ ,  $\kappa_2 = 4.5\kappa_1$ ,  $\omega_1/\kappa_1 = 5 \times 10^6$ .

hence, decreasing  $Q_i$  [39, 40].

In this Letter, we demonstrate that the abovementioned limits can be overcome simultaneously by exploiting the concept of bound states in the continuum (BICs). As a result, high-efficiency H-OPO could be accomplished. BICs were originally proposed by von Neumann and Wigner nearly one century ago in quantum physics and in recent years they have been extended to many other fields [41, 42]. In photonics, BICs can be used to trap light and obtain high- $Q$  modes [43–48], leading to applications such as lasing [49–51], sensing [52, 53] and nonlinear optics [54–59]. Here we implement the Friedrich-Wintgen BICs in an integrated multimode microresonator-waveguide system. As schematically shown in Fig. 1 (c), Friedrich-Wintgen BICs can occur as a result of destructive interference if two near degenerate resonances are dissipatively coupled through a common decay channel [60, 61]. Mathematically, Friedrich-Wintgen BICs are one type of singularity in anti-parity-time symmetric systems [49, 62–67]. To utilize the concept of BICs for the mode number-dependent  $Q$  factor management, we take advantage of the Vernier effect in multimode microresonators (Fig. 1(d)).

We consider an experimental system which consists of a silicon nitride (Si<sub>3</sub>N<sub>4</sub>) microring resonator and an adjacent bus waveguide, as shown in Fig. 2(a). Both the ring and bus waveguide support the higher-order modes TE<sub>10</sub> and TE<sub>20</sub> in addition to the fundamental mode TE<sub>00</sub>. The TE<sub>20</sub> can be ignored in practice because its  $Q$  is much lower. Unlike most widely used microring-waveguide systems, the ring-bus gap here is very small, which allows the fundamental cavity modes to couple with the other (guided and radiation) modes in the bus waveguide besides the fundamental one, see Fig. 2(a).

This results in parasitic loss for the cavity mode and an encompassing reduction in  $Q_i$  and coupling ideality [40]. The role of the bus waveguide on the intrinsic property of microcavities is not sufficiently appreciated [68], but it can have a dramatic influence, especially in multimode cavities [69–71]. In particular, the parasitic loss caused by the bus waveguide can be coherently suppressed when two near resonant cavity modes exist. In this case, Friedrich-Wintgen BICs could emerge because two cavity modes are coupled with the same decay channels. The motion of two near resonant cavity modes can be described by a Schrödinger-type equation (see Supplement Material for more details on the theoretical model and measurements, which includes Refs. [72–75])

$$i\frac{\partial}{\partial t}|\psi\rangle = \mathcal{H}|\psi\rangle + |s\rangle, \quad (1)$$

$$\mathcal{H} = \begin{pmatrix} \omega_1 & g \\ g^* & \omega_2 \end{pmatrix} - i \begin{pmatrix} \kappa_1 & \kappa_{12} \\ \kappa_{12}^* & \kappa_2 \end{pmatrix} - i \begin{pmatrix} \gamma_1 & \sqrt{\gamma_1\gamma_2} \\ \sqrt{\gamma_1\gamma_2} & \gamma_2 \end{pmatrix} \quad (2)$$

with  $|\psi\rangle = [a_1, a_2]^T$ ,  $|s\rangle = [\sqrt{2\gamma_1}, \sqrt{2\gamma_2}]^T s_{\text{in}}$ , where the  $a_{1(2)}$  are the complex amplitudes of the TE<sub>00</sub> and TE<sub>10</sub> cavity modes. In the first term of  $\mathcal{H}$ ,  $\omega_{1(2)}$  are the resonant frequencies in the uncoupled system, and  $g$  is the scattering-induced direct coupling coefficient between the two modes. The second term of  $\mathcal{H}$  is non-Hermitian, where  $\kappa_{1(2)}$  stand for the decay rates caused by intrinsic loss including material absorption, radiation loss and bus-waveguide-induced parasitic loss.  $\kappa_{12}$  denotes the via-the-continuum coupling term since the two cavity modes share the same decay channels. This is the critical parameter for achieving high- $Q_i$  BIC modes. We note that the value of  $\kappa_{12}$  is restricted to  $|\kappa_{12}| < \sqrt{\kappa_1\kappa_2}$  as not all decaying terms can be canceled by perfect destructive

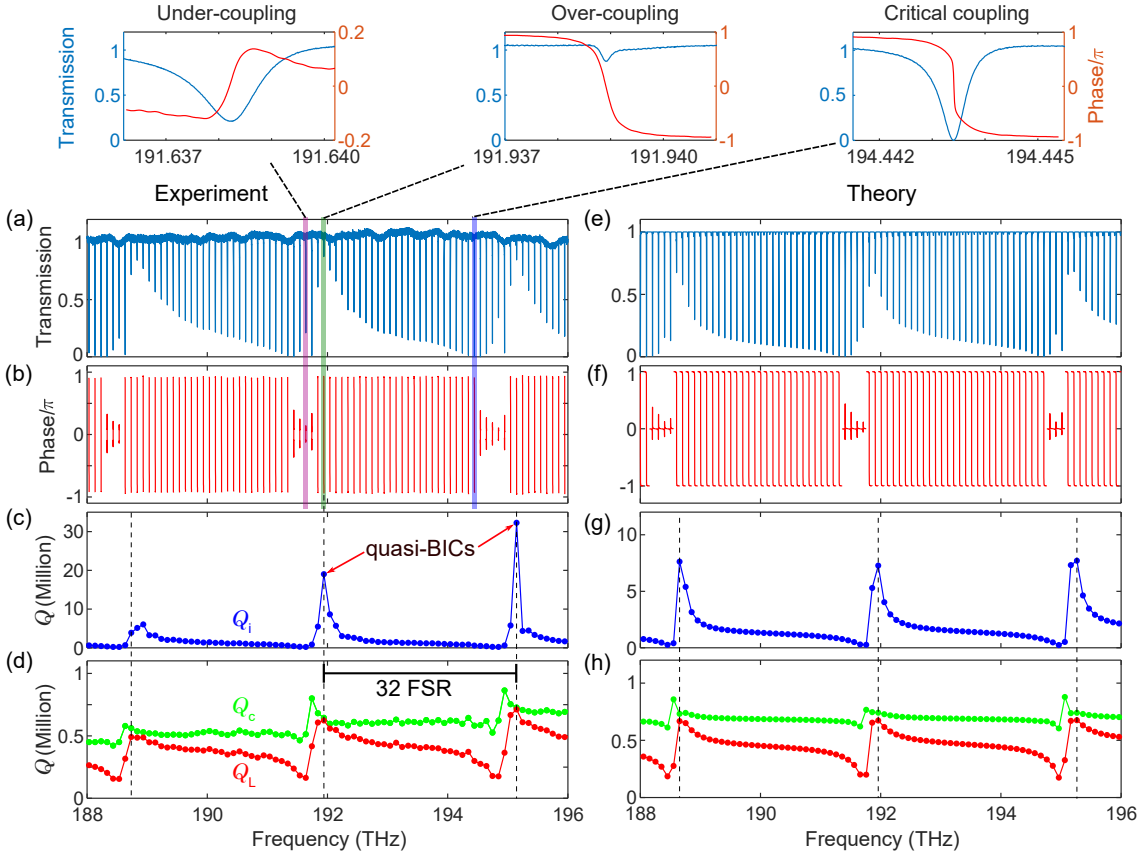


FIG. 3. Observation of BICs via spectral characterization of the system. (a) Normalized transmission scan of the microring-waveguide system. (b) Effective phase response of the system. (c) Intrinsic and (d) coupling as well as loaded  $Q$  factors for the measured resonances. Three coupling conditions: Undercoupling, overcoupling and critical coupling are enlarged in the top panel. (e)-(h) Theoretical results corresponding to the case in panels (a)-(d).

interference, i.e., only quasi-BICs can be attained. The third term of  $\mathcal{H}$  describes the two cavity modes coupling to the fundamental mode of the bus waveguide at rates  $\gamma_{1(2)}$ . The term  $\sqrt{\gamma_1\gamma_2}$  plays a role similar to  $\kappa_{12}$  to generate BICs but it acts on  $Q_c$  instead of  $Q_i$  [44]. It is worth noting that  $Q_i$  and  $Q_c$  play the same role in  $\mathcal{H}$ , but their impact on the light coupling and thus the efficiency of the nonlinear optics process is quite different.

BICs can be obtained from the eigenvalues ( $\omega_{\pm}$ ) of  $\mathcal{H}$ . The real and imaginary parts of the eigenvalues stand for the resonant frequencies and decay rates of two eigenmodes formed by the superposition of the original cavity modes. The quality factors of the two eigenmodes can be calculated by  $Q_{\pm} = |\text{Re}(\omega_{\pm})/2\text{Im}(\omega_{\pm})|$ . Because of coupling, both of the resonant frequencies and decay rates vary with the detuning ( $\omega_1 - \omega_2$ ). To illustrate that  $Q_i$  can be tailored as a result of BICs, we assume  $\gamma_{1(2)} = 0$  and plot the complex frequencies as a function of the detuning, see Fig. 2(b). It is shown that the scattering-induced near field direct coupling ( $g$ ) and via-the-continuum indirect coupling ( $\kappa_{12}$ ) lead to distinct effects on the eigenvalues. The former leads to the real

parts of eigenvalues being avoided and imaginary parts crossed, while the latter gives rise to the opposite effect. Moreover, when only one eigenvalue becomes near purely real, a quasi-BIC is formed at the expense of the other eigenvalue becoming more lossy (its imaginary part increases). In a realistic system, both direct coupling and indirect coupling exist, thus the interference at the coupling region is determined by both. In this scenario, quasi-BICs can still be obtained but, surprisingly at a nonzero detuning, while the  $Q$ s also exhibit asymmetric dependence on the detuning. These aspects will be demonstrated in the following experiment.

The bus waveguide features a tapered structure at both ends to ensure only  $\text{TE}_{00}$  can be excited and collected. The measured normalized transmission spectrum of the system is shown in Fig. 3(a). Unlike the conventional transmission spectrum of a microring-waveguide system, a doubly periodic pattern shows up, given by the nominal FSR of the fundamental mode and a periodic deletion the transmission resonance that arises from the interaction between  $\text{TE}_{00}$  and  $\text{TE}_{10}$  mode families. The period is 32 FSRs of  $\text{TE}_{00}$  mode, which matches the

Vernier frequency corresponding to the walk-off between group indices (see Supplemental Material).

Although two transverse modes families are involved, it is noted that only a single clear resonance dip can be observed within each FSR dominated by  $TE_{00}$  family modes. This can be interpreted as the low- $Q_i$  eigenmodes being extremely undercoupled. Therefore, the transmission spectrum and phase response can be approximately considered as the consequence of single high- $Q_i$  eigenmodes. The measured transmittance and phase allow us to distinguish unambiguously  $Q_i$  and  $Q_c$ , see Fig. 3 and Figure S2 in the Supplemental Material [75].

Following the transmission spectrum, both  $Q_i$  and  $Q_c$  feature periodic patterns but with slightly shifted frequency dependence, which could be explained as the intrinsic loss and coupling loss of cavity modes correspond to different decay channels. As discussed above, due to the coexistence of direct and indirect coupling, both  $Q_i$  and  $Q_c$  as well as the transmission spectrum exhibit a Fano-like frequency dependence. The asymmetric  $Q$  distribution with respect to pump mode further reduces the risk of mode competition in H-OPO as demonstrated in the following section. In addition to suppressing mode competition, another advantage of engineering  $Q_i$  is that the modes with highest  $Q_L$  are strongly overcoupled (top panel of Fig. 3). This counterintuitive phenomenon is especially important for achieving high-efficiency nonlinear optics phenomena, and H-OPO in particular.

The above theoretical model only considers the interaction between a pair of near resonant modes. To better describe the realistic system over a wider spectral range, we have generalized the above model to four interacting modes (Supplemental Material) by including the effect that one mode from  $TE_{00}$  family could couple to more than one mode from the  $TE_{10}$  family simultaneously and vice versa, see Figs. 3(e)-(h). The good match between theory and experiment suggests our model captures the main underlying physics of the system.

To generate H-OPO, anomalous dispersion is required. We found the supermode's dispersion is dominated by the  $TE_{00}$  mode with mode-interaction-induced distortion (see Supplemental Material). To pump this device, we use a laser located at 1561.9 nm after being amplified by an erbium-doped fiber amplifier. The on-chip pump power threshold of this H-OPO is  $\sim 60$  mW, and the highest conversion efficiency is attained at 200 mW. To couple pump into resonance, we decrease laser's frequency gradually. With more pump power coupled into the microresonator, a pair of signal and idler waves are generated, exactly located at the quasi-BIC locations, see Fig. 4(a). With further decreasing the pump frequency, the power of signal and idler increases linearly before reaching saturation (see Fig. 4(b)). The maximum conversion efficiency  $\eta_s = (P_s + P_i)/P_0 = 68\%$ , corresponding to  $\sim 70$  mW on-chip signal power. The value could be further improved if the undesired BICs (i.e. BICs modes ex-

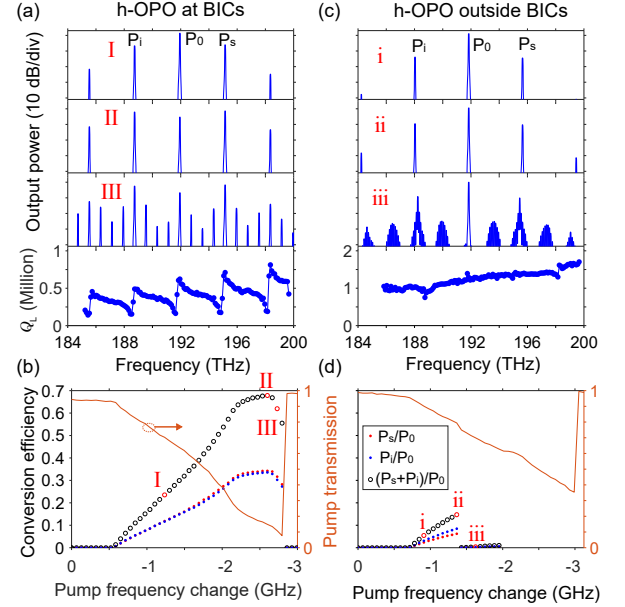


FIG. 4. Experimental demonstration of H-OPO in microresonators at and outside BICs. (a) Measured optical spectra at different pump-cavity detunings. As a reference, frequency-dependent loaded  $Q$  ( $Q_L$ ) is plotted at the bottom. (b) Calculated conversion efficiency and pump transmission as a function of the pump frequency. (c)-(d) same as (a)-(b) except for pumping another sample.

cluding pump, signal and idler modes) and the resultant cascaded four-wave mixing were suppressed (Supplemental Material), for example, by coupling with an auxiliary cavity [76]. By further reducing the detuning, the conversion efficiency decreases suddenly as a result of the birth of new lines, indicating the low- $Q$  modes can still be activated at high pump power. The advantage of BICs can be clearly shown if we pump another sample, which has the same geometric parameters except for 50 nm larger ring-bus gap. Hence, it does not feature quasiperiod  $Q$  response and the highest conversion efficiency is limited to  $< 15\%$  due to mode competition.

To conclude, we have implemented BICs in an integrated Kerr nonlinear microring resonator featuring a high-contrast quasiperiodic response in quality factor. By exploring waveguide-assisted dissipative mode coupling in microring-waveguide system, we generalize the spectral response and demonstrate the feasibility of boosting  $Q_i$  in high- $Q$  microresonators. Such a simple system not only enables the unwanted modes to be suppressed, but it also allows to obtain strong overcoupling without sacrificing  $Q_i$  for desired modes. The  $Q_i$  can in fact be higher than in standard single-mode systems, resulting in unprecedented efficiency in H-OPO and high-power signal and idler waves. Besides H-OPO, the possibility to engineer the spectral response of the intrinsic quality factor of high- $Q$  microresonators can be useful for

other power-efficient nonlinear optics scenarios, and the strong overcoupling (high  $Q_i/Q_c$ ) could especially facilitate the generation of squeezed or entangled states of light [8, 76–79].

The devices demonstrated in this work were fabricated at Myfab Chalmers. This work was supported by European Research Council (CoG GA 771410); Vetenskapsrådet (2020-00453). The raw data for this work can be accessed at <https://doi.org/10.5281/zenodo.7529404>.

## THEORY

### Two-mode model

The Hamiltonian of a two-mode (one TE<sub>00</sub> and one TE<sub>10</sub>) microresonator coupled with a bus waveguide system reads ( $\hbar = 1$ )

$$\begin{aligned} \mathbf{H} = & \sum_{k=1,2} \omega_k a_k^\dagger a_k + (g a_1^\dagger a_2 + g^* a_2^\dagger a_1) + \int_{-\infty}^{\infty} \omega b^\dagger(\omega) b(\omega) d\omega \\ & + \sum_j \int_{-\infty}^{\infty} \omega c_j^\dagger(\omega) c_j(\omega) d\omega \\ & + \sum_{k=1,2} \int_{-\infty}^{\infty} d\omega [\eta_k(\omega) a_k^\dagger b(\omega) + \eta_k^*(\omega) a_k b^\dagger(\omega)] \\ & + \sum_{k=1,2} \sum_j \int_{-\infty}^{\infty} d\omega [\lambda_{kj}(\omega) a_k^\dagger c_j(\omega) + \lambda_{kj}^*(\omega) a_k c_j^\dagger(\omega)], \end{aligned}$$

where  $a_k[a_k^\dagger]$  is the annihilation (creation) operator of the  $k$ th cavity mode, whose resonant frequency is  $\omega_k$ .  $g$  is the scattering-induced (e.g., roughness induced scattering) direct coupling coefficient between the two cavity modes.  $b(\omega)[b^\dagger(\omega)]$  and  $c_j(\omega)[c_j^\dagger(\omega)]$  denote the annihilation (creation) operator of the fundamental mode of bus waveguide (TE<sub>00</sub>) and  $j$ th other modes (all guided modes of the bus waveguide except for TE<sub>00</sub> and radiation modes), which are coupled with  $k$ th cavity mode with coupling coefficients  $\eta_k$  and  $\lambda_{kj}$  respectively.

The Heisenberg equations of motion for the cavity and waveguide modes are

$$\begin{aligned} \frac{da_1}{dt} = & -i\omega_1 a_1 - i g a_2 - i \int_{-\infty}^{\infty} d\omega \eta_1(\omega) b(\omega) \\ & - i \sum_j \int_{-\infty}^{\infty} d\omega \lambda_{1,j}(\omega) c_j(\omega), \end{aligned} \quad (\text{S.1})$$

$$\begin{aligned} \frac{da_2}{dt} = & -i\omega_2 a_2 - i g^* a_1 - i \int_{-\infty}^{\infty} d\omega \eta_2(\omega) b(\omega) \\ & - i \sum_j \int_{-\infty}^{\infty} d\omega \lambda_{2,j}(\omega) c_j(\omega), \end{aligned} \quad (\text{S.2})$$

$$\frac{db(\omega)}{dt} = -i\omega b(\omega) - i \sum_{k=1,2} \eta_k^*(\omega) a_k, \quad (\text{S.3})$$

$$\frac{dc_j(\omega)}{dt} = -i\omega c_j(\omega) - i \sum_{k=1,2} \lambda_{k,j}^*(\omega) a_k. \quad (\text{S.4})$$

By integrating Eqs. (S.3-S.4), we obtain

$$b(\omega) = b^0(\omega) e^{-i\omega(t-t_0)} - i \sum_{k=1,2} \eta_k^*(\omega) \int_{t_0}^t e^{-i\omega(t-t')} a_k(t') dt', \quad (\text{S.5})$$

the phase of  $a_k$ ), Eqs. (S.7)-(S.8) can be reduced as

$$c_j(\omega) = c_j^0(\omega)e^{-i\omega(t-t_0)} - i \sum_{k=1,2} \lambda_{k,j}^*(\omega) \int_{t_0}^t e^{-i\omega(t-t')} a_k(t') dt', \quad -\kappa_{11}a_1 - \kappa_{12}a_2 - ic_{1,\text{in}}, \quad (S.9)$$

$$(S.6)$$

where  $b^0(\omega)$  and  $c_j^0(\omega)$  are the values of  $b(\omega)$  and  $c_j(\omega)$  at  $t = t_0$ . Bring Eqs. (S.5)-(S.6) into Eqs. (S.1)-(S.2), and we have

$$\begin{aligned} \frac{da_1}{dt} &= -i\omega_1 a_1 - i g a_2 - i \int_{-\infty}^{\infty} d\omega \eta_1(\omega) e^{-i\omega(t-t_0)} b^0(\omega) \\ &- \int_{-\infty}^{\infty} d\omega \eta_1(\omega) \sum_{k=1,2} \eta_k^*(\omega) \int_{t_0}^t e^{-i\omega(t-t')} a_k(t') dt' \\ &- i \sum_j \int_{-\infty}^{\infty} d\omega \lambda_{1,j}(\omega) e^{-i\omega(t-t_0)} c_j^0(\omega) \\ &- \sum_j \int_{-\infty}^{\infty} d\omega \lambda_{1,j}(\omega) \sum_{k=1,2} \lambda_{k,j}^*(\omega) \int_{t_0}^t e^{-i\omega(t-t')} a_k(t') dt', \end{aligned} \quad (S.7)$$

$$\begin{aligned} \frac{da_2}{dt} &= -i\omega_2 a_2 - i g^* a_1 - i \int_{-\infty}^{\infty} d\omega \eta_2(\omega) e^{-i\omega(t-t_0)} b^0(\omega) \\ &- \int_{-\infty}^{\infty} d\omega \eta_2(\omega) \sum_{k=1,2} \eta_k^*(\omega) \int_{t_0}^t e^{-i\omega(t-t')} a_k(t') dt' \\ &- i \sum_j \int_{-\infty}^{\infty} d\omega \lambda_{2,j}(\omega) e^{-i\omega(t-t_0)} c_j^0(\omega) \\ &- \sum_j \int_{-\infty}^{\infty} d\omega \lambda_{2,j}(\omega) \sum_{k=1,2} \lambda_{k,j}^*(\omega) \int_{t_0}^t e^{-i\omega(t-t')} a_k(t') dt'. \end{aligned} \quad (S.8)$$

Using first-Markov approximation [72, 73], i.e., assuming  $\eta_k$  and  $\lambda_{k,j}$  to be constant as a function of  $\omega$  (for convenience,  $\eta_k$  can be assumed to be real by properly defining

$$\begin{aligned} \frac{da_2}{dt} &= -i\omega_2 a_2 - i g^* a_1 - \gamma_2 a_2 - \sqrt{\gamma_1 \gamma_2} a_1 - i \sqrt{2\gamma_2} s_{\text{in}} \\ &- \kappa_2 a_2 - \kappa_{12}^* a_1 - i c_{2,\text{in}}, \end{aligned} \quad (S.10)$$

where  $\gamma_k = |\eta_k|^2/2$ ,  $\kappa_k = \sum_j |\lambda_{k,j}|^2/2$ ,  $\kappa_{12} = \sum_j \lambda_{1,j} \lambda_{2,j}^*/2$ ,  $s_{\text{in}} = \int_{-\infty}^{\infty} d\omega e^{-i\omega(t-t_0)} b^0(\omega)$ ,  $c_{k,\text{in}} = \sum_j \lambda_{k,j} \int_{-\infty}^{\infty} d\omega e^{-i\omega(t-t_0)} c_j^0(\omega)$ .  $s_{\text{in}}$  and  $c_{k,\text{in}}$  stand for the input field of the  $k$ th cavity mode. In the classical case,  $c_{k,\text{in}}$  can be ignored because the input field is only applied to the  $\text{TE}_{00}$  of the bus waveguide. In addition, the material absorption and ring bending radiation induced cavity decay should be considered, which can be included into  $\kappa_{1,2}$  since they are treated as the intrinsic decay rate. It is easy to see  $|\kappa_{12}| < \sqrt{\kappa_1 \kappa_2}$ . Equations. (S.9-S.10) can be expressed in the compact form, given by Eqs (1)-(2).

#### Four-mode model

The above two-mode model captures the main underlying physics of BICs. However, it is incapable of reconstructing the transmission spectrum with a span beyond one Vernier period (32 FSRs). Owing to the Vernier effect, one  $\text{TE}_{00}$  cavity mode could be equally coupled with two neighbouring longitudinal  $\text{TE}_{10}$  modes when its resonance frequency is in the middle. To generate a transmission spectrum with a span of three Vernier periods, we generalize the two-mode model to four-modes, where one  $\text{TE}_{00}$  mode simultaneously couples with three neighboring longitudinal modes of  $\text{TE}_{10}$  family, as illustrated in Figure S1(a). To be specific, we render  $j$ th ( $j = 1, 2, 3..$  from left to right)  $\text{TE}_{00}$  mode couple with  $j$ th,  $j+1$ th and  $j+2$ th  $\text{TE}_{10}$  modes simultaneously, and set the 1st  $\text{TE}_{00}$  mode to be red-detuned from the 1st  $\text{TE}_{10}$  mode. Such arrangement warrants one  $\text{TE}_{00}$  mode could couple with at least one  $\text{TE}_{10}$  mode with detuning less than 0.5 FSR, thus the feature of the transmission response can be well captured.

The coupled mode equations for the four-mode model can be directly generalized from Eqs. (1)-(2) as

$$i \frac{d}{dt} \begin{pmatrix} a \\ b_1 \\ b_2 \\ b_3 \end{pmatrix} = \mathcal{H} \begin{pmatrix} a \\ b_1 \\ b_2 \\ b_3 \end{pmatrix} + \begin{pmatrix} \sqrt{2\gamma_a} \\ \sqrt{2\gamma_b} \\ \sqrt{2\gamma_b} \\ \sqrt{2\gamma_b} \end{pmatrix} s_{\text{in}}, \quad (S.11)$$

$$\mathcal{H} = \begin{pmatrix} \omega_a & g & g & g \\ g^* & \omega_{b1} & 0 & 0 \\ g^* & 0 & \omega_{b2} & 0 \\ g^* & 0 & 0 & \omega_{b3} \end{pmatrix} - i \begin{pmatrix} \kappa_a + \gamma_a & \kappa_{ab} + \sqrt{\gamma_a \gamma_b} & \kappa_{ab} + \sqrt{\gamma_a \gamma_b} & \kappa_{ab} + \sqrt{\gamma_a \gamma_b} \\ \kappa_{ab}^* + \sqrt{\gamma_a \gamma_b} & \kappa_b + \gamma_b & \kappa_{bb} + \gamma_b & \kappa_{bb} + \gamma_b \\ \kappa_{ab}^* + \sqrt{\gamma_a \gamma_b} & \kappa_b^* + \gamma_b & \kappa_b + \gamma_b & \kappa_{bb} + \gamma_b \\ \kappa_{ab}^* + \sqrt{\gamma_a \gamma_b} & \kappa_b^* + \gamma_b & \kappa_b^* + \gamma_b & \kappa_b + \gamma_b \end{pmatrix}, \quad (\text{S.12})$$

where  $a$  stands for the  $\text{TE}_{00}$  mode and  $b_{1,2,3}$  correspond to three  $\text{TE}_{10}$  adjacent longitudinal modes. The coefficients  $\omega$ ,  $g$ ,  $\gamma$  and  $\kappa$  take on the similar physical meaning in the two-mode model.

The transmission spectrum around each  $\text{TE}_{00}$  resonances can be obtained  $T = |s_{\text{out}}/s_{\text{in}}|^2$  with  $s_{\text{out}}$  being determined from cavity input-output relation [72]

$$s_{\text{out}} = s_{\text{in}} - i\sqrt{2\gamma_a}a - i\sqrt{2\gamma_b}b_1 - i\sqrt{2\gamma_b}b_2 - i\sqrt{2\gamma_b}b_3. \quad (\text{S.13})$$

To obtain the  $Q_i$  and  $Q_L$  of the high- $Q$  supermode, we use a Lorentz function to fit the deepest dip in the transmission spectrum. The phase response can be directly calculated from the transmission coefficient  $s_{\text{out}}/s_{\text{in}}$ . The broadband transmission spectrum is formed by combing each individual spectrum.

The parameters used for Fig. 3 are  $\gamma_a/2\pi = 140$  MHz,  $\gamma_b/2\pi = 10$  MHz,  $\kappa_a/2\pi = 70$  MHz,  $\kappa_b/2\pi = 1.7$  GHz,  $g/2\pi = -900$  MHz,  $\kappa_{ab}/2\pi = 320$  MHz,  $\kappa_{bb}/2\pi = 1.6$  GHz.

We emphasize the four-mode model and two-mode model only give little difference within one Vernier period. In Figure 5(b), we show a comparison of the spectral response given by the two-mode model and four-mode model. We can see both predict quasi-BICs but with slight difference in transmission spectra and quality factors.

## DEVICE FABRICATION AND CHARACTERIZATION

The devices were fabricated on a silicon wafer using a subtractive processing method [74]. The light is coupled into and out the chip using two lensed fibers with 5 dB coupling loss in total. The devices were characterized by a tunable external cavity laser whose frequency is precisely measured by a frequency comb-calibrated fiber interferometer. To obtain the resonance parameters and untangle undercoupling and overcoupling unambiguously, the complex transmission coefficient  $t = \sqrt{T}e^{i\phi}$  was measured around each resonance, where  $T$  is transmittance and  $\phi$  is the phase. The phase is measured from swept-wavelength interference pattern, see Figure 6 [75]. For each individual resonance, the measured  $t$  as a function of laser frequency is fitted by

$$t = 1 + \frac{\kappa_c}{i(\omega - \omega_0) - \frac{\kappa_c + \kappa_0}{2} + \frac{\kappa_1^2}{i(\omega - \omega_0) - \frac{\kappa_c + \kappa_0}{2}}}, \quad (\text{S.14})$$

which is obtained from steady-state temporal coupled mode theory including back-scattering induced coupling (with coefficient  $\kappa_i$ ) between two degenerate counter-propagating modes. The evaluated coupling coefficients of the resonances enable calculating the quality factors:  $Q_i = \omega_0/\kappa_i$ ,  $Q_c = \omega_0/\kappa_c$ , and  $Q_L = \omega_0/(\kappa_i + \kappa_c)$ .

## VERNIER EFFECT IN TRANSMISSION SPECTRUM

The observed double periodicity of transmission response in Fig. 3 can be attributed to the interaction between  $\text{TE}_{00}$  and  $\text{TE}_{10}$  mode families as the calculated Vernier period matches with the observation:  $f_V/\text{FSR}(\text{TE}_{00}) = n_g(\text{TE}_{00})/[n_g(\text{TE}_{10}) - n_g(\text{TE}_{00})] = 2.088/(2.154 - 2.088) = 31.6$ . Here  $n_g$  is the group index simulated by COMSOL with measured material and geometric parameters.

To obtain the FSRs of both  $\text{TE}_{00}$  and  $\text{TE}_{10}$  modes in the ring resonator experimentally, we measure another sample with the same dimension of ring but different width of bus waveguide (1200 nm) and ring-bus gap (600 nm), as a result, both the two mode families can be directly observed, see Figure S3. The two families can be easily distinguished. The measured FSRs are 100.28 GHz and 97.18 GHz, which gives the Vernier period to be  $f_V/\text{FSR}(\text{TE}_{00}) = \text{FSR}(\text{TE}_{10})/[\text{FSR}(\text{TE}_{00}) - \text{FSR}(\text{TE}_{10})] = 31.3$ . Again, it matches with the pattern period in Fig. 3.

## MORE INFORMATION ABOUT MICRORING-WAVEGUIDE SAMPLES

The dispersion of the cavity modes is characterized by the integrated dispersion  $D_{\text{int}}$ :

$$D_{\text{int}} = \omega_\mu - (\omega_0 + \mu D_1), \quad (\text{S.15})$$

where  $\omega_\mu$  is the resonant frequency of  $\mu$ th longitudinal mode counting from the pump resonance.  $D_1/2\pi$  is the microresonator FSR. By fitting  $D_{\text{int}}$  (Figure 8(a)), we obtained the group velocity dispersion  $\beta_2 = -46\text{ps}^2/\text{km}$  for the sample used for Fig. 3 and Fig. 4(a)-(b) in the main text. For comparison, the dispersion of another sample used for Fig. 4(c)-(d) in the main text is plotted in Figure 8(b). The two samples feature the same geometry except for microring-waveguide gap. By comparison, we can see  $D_{\text{int}}$  is dominated by  $\text{TE}_{00}$  mode family. This also sug-



gests the measured high- $Q$  resonances are dominated by  $TE_{00}$  modes with perturbation by  $TE_{10}$  modes.

The linear characterization of the sample used for Fig. 4(c)-(d) in the main text is shown in Figure 9. Same as Fig. 3, the transmission spectrum and phase response are measured for the analysis of the quality factors. Comparing to Fig. 3, the BICs ( $Q$ -contrast) here is much weaker ( $Q_i$  value at regimes outside BICs is high), especially at the short wavelength region. This could be attributed to the reduced mode coupling among the modes. As a result, the parasitic mode competition cannot be efficiently suppressed, and the parametric oscillation can only reaches up to 14.6% in conversion efficiency though the cavity modes are still in the strong over-coupling condition ( $Q_i/Q_c > 10$ ).

### H-OPO CONVERSION EFFICIENCY ANALYSIS

In this section, we numerically study the conversion efficiency in h-OPO. The maximal conversion efficiency in h-OPO is ultimately determined by the quality factors of microresonators [26]:

$$\eta_{\max} = \left( \frac{Q_i/Q_c}{1 + Q_i/Q_c} \right)^2, \quad (\text{S.16})$$

where the signal, idler and pump modes are assumed to feature the same  $Q_i$  and  $Q_c$ . This theoretical limit is derived based on three-mode approximation, i.e., only signal, idler and pump modes are considered for interaction. To reach the theoretical maximum, proper parameters such as dispersion, detuning, pump power should be optimized in addition to quality factors.

By choosing: FSR=100.16 GHz,  $Q_c = 0.8 \times 10^6$ , group velocity dispersion  $\beta_2 = -46\text{ps}^2/\text{km}$ , nonlinear coefficient of microring waveguide  $\gamma = 0.76\text{W}^{-1}\text{m}^{-1}$ , pump power  $P_0 = 21$  dBm, and different  $Q_i$  for active modes (see below), we performed a series of numerical simulations of the conversion efficiency in h-OPO, see Figure 10. The conversion efficiency in the plot represents the maximum value regarding to the pump-cavity detuning.

The simulations were performed with an Ikeda map of a Kerr microresonator-waveguide system, where 512 cavity modes were considered. To perform three-mode simulation, we inactivate all modes (by setting their  $Q_i$  to be 0) except for mode -32, 0, 32 (counted from pump mode). As a result, only the three modes can be effectively excited and the conversion efficiency can be achieved to be close to the theoretical maximum.

To simulate our microresonator with BICs, the modes with number  $n \times 32$  are turned to be active ( $n = \pm 1, 2, 3, \dots$ ). In this case, high-efficient coherent h-OPO can still be generated but slightly (typically few percent) lower than the three-mode case, which can be explained as partial power is lost into high-order sidebands through four-wave mixing process.

If 512 cavity modes are activated, i.e., multi-mode case, the maximum conversion efficiency is lower, which is not mainly limited by quality factors but by mode competition, see Figure 10(b).

These analyses demonstrate that the use of BICs can get the conversion efficiency in realistic multi-mode systems closer to the ideal situation of a pure three-wave h-OPO.

---

\* torresv@chalmers.se

- [1] P. Del'Haye, A. Schliesser, O. Arcizet, T. Wilken, R. Holzwarth, and T. J. Kippenberg, Optical frequency comb generation from a monolithic microresonator, *Nature* **450**, 1214 (2007).
- [2] T. J. Kippenberg, S. M. Spillane, and K. J. Vahala, Kerr-nonlinearity optical parametric oscillation in an ultrahigh- $Q$  toroid microcavity, *Phys. Rev. Lett.* **93**, 083904 (2004).
- [3] A. A. Savchenkov, A. B. Matsko, D. Strekalov, M. Mohageg, V. S. Ilchenko, and L. Maleki, Low threshold optical oscillations in a whispering gallery mode  $\text{CaF}_2$  resonator, *Phys. Rev. Lett.* **93**, 243905 (2004).
- [4] C. Y. Wang, T. Herr, P. Del'Haye, A. Schliesser, J. Hofer, R. Holzwarth, T. Hänsch, N. Picqué, and T. J. Kippenberg, Mid-infrared optical frequency combs at  $2.5 \mu\text{m}$  based on crystalline microresonators, *Nat. Commun.* **4**, 1345 (2013).
- [5] Y. Yang, X. Jiang, S. Kasumie, G. Zhao, L. Xu, J. M. Ward, L. Yang, and S. Nic Chormaic, Four-wave mixing parametric oscillation and frequency comb generation at visible wavelengths in a silica microbubble resonator, *Opt. Lett.* **41**, 5266 (2016).
- [6] X. Shen, R. C. Beltran, V. M. Diep, S. Soltani, and A. M. Armani, Low-threshold parametric oscillation in organically modified microcavities, *Sci. Adv.* **4**, eaao4507 (2018).
- [7] K. Tian, J. Yu, F. Lei, J. Ward, A. Li, P. Wang, and S. Nic Chormaic, Blue band nonlinear optics and photodarkening in silica microdevices, *Photon. Res.* **10**, 2073 (2022).
- [8] A. Dutt, K. Luke, S. Manipatruni, A. L. Gaeta, P. Nussenzveig, and M. Lipson, On-chip optical squeezing, *Phys. Rev. Appl.* **3**, 044005 (2015).
- [9] Y. K. Chembo, Quantum dynamics of Kerr optical frequency combs below and above threshold: Spontaneous four-wave mixing, entanglement, and squeezed states of light, *Phys. Rev. A* **93**, 033820 (2016).
- [10] M. Kues, C. Reimer, P. Roztock, L. R. Cortés, S. Sciara, B. Wetzel, Y. Zhang, A. Cino, S. T. Chu, B. E. Little, *et al.*, On-chip generation of high-dimensional entangled quantum states and their coherent control, *Nature* **546**, 622 (2017).
- [11] P. Imany, J. A. Jaramillo-Villegas, O. D. Odele, K. Han, D. E. Leaird, J. M. Lukens, P. Lougovski, M. Qi, and A. M. Weiner, 50-GHz-spaced comb of high-dimensional frequency-bin entangled photons from an on-chip silicon nitride microresonator, *Opt. Express* **26**, 1825 (2018).
- [12] A. B. Matsko, Hyperparametric frequency noise eater, *Phys. Rev. A* **99**, 023843 (2019).



- [13] X. Lu, Q. Li, D. A. Westly, G. Moille, A. Singh, V. Anant, and K. Srinivasan, Chip-integrated visible-telecom entangled photon pair source for quantum communication, *Nat. Phys.* **15**, 373 (2019).
- [14] Y. Okawachi, M. Yu, J. K. Jang, X. Ji, Y. Zhao, B. Y. Kim, M. Lipson, and A. L. Gaeta, Demonstration of chip-based coupled degenerate optical parametric oscillators for realizing a nanophotonic spin-glass, *Nat. Commun.* **11**, 4119 (2020).
- [15] G. Lin, A. Coillet, and Y. K. Chembo, Nonlinear photonics with high- $Q$  whispering-gallery-mode resonators, *Adv. Opt. Photonics* **9**, 828 (2017).
- [16] Y. Li, X. Jiang, G. Zhao, and L. Yang, Whispering gallery mode microresonator for nonlinear optics, *arXiv preprint arXiv:1809.04878* (2018).
- [17] J. S. Levy, A. Gondarenko, M. A. Foster, A. C. Turner-Foster, A. L. Gaeta, and M. Lipson, CMOS-compatible multiple-wavelength oscillator for on-chip optical interconnects, *Nat. Photonics* **4**, 37 (2010).
- [18] L. Razzari, D. Duchesne, M. Ferrera, R. Morandotti, S. Chu, B. Little, and D. Moss, CMOS-compatible integrated optical hyper-parametric oscillator, *Nat. Photonics* **4**, 41 (2010).
- [19] B. Hausmann, I. Bulu, V. Venkataraman, P. Deotare, and M. Lončar, Diamond nonlinear photonics, *Nat. Photonics* **8**, 369 (2014).
- [20] M. Pu, L. Ottaviano, E. Semenova, and K. Yvind, Efficient frequency comb generation in AlGaAs-on-insulator, *Optica* **3**, 823 (2016).
- [21] Q. Li, M. Davanço, and K. Srinivasan, Efficient and low-noise single-photon-level frequency conversion interfaces using silicon nanophotonics, *Nat. Photonics* **10**, 406 (2016).
- [22] X. Ji, F. A. Barbosa, S. P. Roberts, A. Dutt, J. Cardenas, Y. Okawachi, A. Bryant, A. L. Gaeta, and M. Lipson, Ultra-low-loss on-chip resonators with sub-milliwatt parametric oscillation threshold, *Optica* **4**, 619 (2017).
- [23] Y. Tang, Z. Gong, X. Liu, and H. X. Tang, Widely separated optical Kerr parametric oscillation in AlN microrings, *Opt. Lett.* **45**, 1124 (2020).
- [24] C. Wang, Z. Fang, A. Yi, B. Yang, Z. Wang, L. Zhou, C. Shen, Y. Zhu, Y. Zhou, R. Bao, *et al.*, High- $Q$  microresonators on 4H-silicon-carbide-on-insulator platform for nonlinear photonics, *Light Sci. Appl.* **10**, 139 (2021).
- [25] G. Marty, S. Combrié, F. Raineri, and A. De Rossi, Photonic crystal optical parametric oscillator, *Nat. Photonics* **15**, 53 (2021).
- [26] N. L. B. Sayson, T. Bi, V. Ng, H. Pham, L. S. Trainor, H. G. Schwefel, S. Coen, M. Erkintalo, and S. G. Murdoch, Octave-spanning tunable parametric oscillation in crystalline Kerr microresonators, *Nat. Photonics* **13**, 701 (2019).
- [27] S. Fujii, S. Tanaka, M. Fuchida, H. Amano, Y. Hayama, R. Suzuki, Y. Kakinuma, and T. Tanabe, Octave-wide phase-matched four-wave mixing in dispersion-engineered crystalline microresonators, *Opt. Lett.* **44**, 3146 (2019).
- [28] X. Lu, G. Moille, A. Singh, Q. Li, D. A. Westly, A. Rao, S.-P. Yu, T. C. Briles, S. B. Papp, and K. Srinivasan, Milliwatt-threshold visible-telecom optical parametric oscillation using silicon nanophotonics, *Optica* **6**, 1535 (2019).
- [29] X. Lu, G. Moille, A. Rao, D. A. Westly, and K. Srinivasan, On-chip optical parametric oscillation into the visible: generating red, orange, yellow, and green from a near-infrared pump, *Optica* **7**, 1417 (2020).
- [30] R. R. Domenegueti, Y. Zhao, X. Ji, M. Martinelli, M. Lipson, A. L. Gaeta, and P. Nussenzveig, Parametric sideband generation in CMOS-compatible oscillators from visible to telecom wavelengths, *Optica* **8**, 316 (2021).
- [31] J. R. Stone, G. Moille, X. Lu, and K. Srinivasan, Conversion efficiency in Kerr-microresonator optical parametric oscillators: From three modes to many modes, *Phys. Rev. Appl.* **17**, 024038 (2022).
- [32] S. Radic, Parametric amplification and processing in optical fibers, *Laser Photonics Rev.* **2**, 498 (2008).
- [33] Z. Ye, P. Zhao, K. Twayana, M. Karlsson, V. Torres-Company, and P. A. Andrekson, Overcoming the quantum limit of optical amplification in monolithic waveguides, *Sci. Adv.* **7**, eabi8150 (2021).
- [34] T. Herr, K. Hartinger, J. Riemensberger, C. Wang, E. Gavartin, R. Holzwarth, M. Gorodetsky, and T. Kippenberg, Universal formation dynamics and noise of Kerr-frequency combs in microresonators, *Nat. Photonics* **6**, 480 (2012).
- [35] V. Torres-Company, D. Castelló-Lurbe, and E. Silvestre, Comparative analysis of spectral coherence in microresonator frequency combs, *Opt. Express* **22**, 4678 (2014).
- [36] B. P.-P. Kuo, J. M. Fini, L. Grüner-Nielsen, and S. Radic, Dispersion-stabilized highly-nonlinear fiber for wideband parametric mixer synthesis, *Opt. Express* **20**, 18611 (2012).
- [37] C. M. Gentry, X. Zeng, and M. A. Popović, Tunable coupled-mode dispersion compensation and its application to on-chip resonant four-wave mixing, *Opt. Lett.* **39**, 5689 (2014).
- [38] X. Lu, A. McClung, and K. Srinivasan, High- $Q$  slow light and its localization in a photonic crystal microring, *Nature Photonics* **16**, 66 (2022).
- [39] D. T. Spencer, J. F. Bauters, M. J. Heck, and J. E. Bowers, Integrated waveguide coupled  $\text{Si}_3\text{N}_4$  resonators in the ultrahigh- $Q$  regime, *Optica* **1**, 153 (2014).
- [40] M. H. P. Pfeiffer, J. Liu, M. Geiselmann, and T. J. Kippenberg, Coupling ideality of integrated planar high- $Q$  microresonators, *Phys. Rev. Appl.* **7**, 024026 (2017).
- [41] C. W. Hsu, B. Zhen, A. D. Stone, J. D. Joannopoulos, and M. Soljačić, Bound states in the continuum, *Nat. Rev. Mater.* **1**, 16048 (2016).
- [42] S. I. Azzam and A. V. Kildishev, Photonic bound states in the continuum: from basics to applications, *Adv. Opt. Mater.* **9**, 2001469 (2021).
- [43] T. Lepetit, E. Akmanşoy, J.-P. Ganne, and J.-M. Lourtioz, Resonance continuum coupling in high-permittivity dielectric metamaterials, *Phys. Rev. B* **82**, 195307 (2010).
- [44] C. M. Gentry and M. A. Popović, Dark state lasers, *Opt. Lett.* **39**, 4136 (2014).
- [45] C.-L. Zou, J.-M. Cui, F.-W. Sun, X. Xiong, X.-B. Zou, Z.-F. Han, and G.-C. Guo, Guiding light through optical bound states in the continuum for ultrahigh- $Q$  microresonators, *Laser Photonics Rev.* **9**, 114 (2015).
- [46] M. V. Rybin, K. L. Koshelev, Z. F. Sadrieva, K. B. Samusev, A. A. Bogdanov, M. F. Limonov, and Y. S. Kivshar, High- $Q$  supercavity modes in subwavelength dielectric resonators, *Phys. Rev. Lett.* **119**, 243901 (2017).
- [47] E. A. Bezus, D. A. Bykov, and L. L. Doskolovich, Bound states in the continuum and high- $Q$  resonances supported

- by a dielectric ridge on a slab waveguide, *Photon. Res.* **6**, 1084 (2018).
- [48] Z. Yu, X. Xi, J. Ma, H. K. Tsang, C.-L. Zou, and X. Sun, Photonic integrated circuits with bound states in the continuum, *Optica* **6**, 1342 (2019).
- [49] H. Hodaie, A. Hassan, W. Hayenga, M. Miri, D. Christodoulides, and M. Khajavikhan, Dark-state lasers: mode management using exceptional points, *Opt. Lett.* **41**, 3049 (2016).
- [50] A. Kodigala, T. Lepetit, Q. Gu, B. Bahari, Y. Fainman, and B. Kanté, Lasing action from photonic bound states in continuum, *Nature* **541**, 196 (2017).
- [51] C. Huang, C. Zhang, S. Xiao, Y. Wang, Y. Fan, Y. Liu, N. Zhang, G. Qu, H. Ji, J. Han, *et al.*, Ultrafast control of vortex microlasers, *Science* **367**, 1018 (2020).
- [52] A. A. Yanik, A. E. Cetin, M. Huang, A. Artar, S. H. Mousavi, A. Khanikaev, J. H. Connor, G. Shvets, and H. Altug, Seeing protein monolayers with naked eye through plasmonic Fano resonances, *Proc. Natl. Acad. Sci. U.S.A.* **108**, 11784 (2011).
- [53] B. Zhen, S.-L. Chua, J. Lee, A. W. Rodriguez, X. Liang, S. G. Johnson, J. D. Joannopoulos, M. Soljačić, and O. Shapira, Enabling enhanced emission and low-threshold lasing of organic molecules using special Fano resonances of macroscopic photonic crystals, *Proc. Natl. Acad. Sci. U.S.A.* **110**, 13711 (2013).
- [54] L. Carletti, K. Koshelev, C. De Angelis, and Y. Kivshar, Giant nonlinear response at the nanoscale driven by bound states in the continuum, *Phys. Rev. Lett.* **121**, 033903 (2018).
- [55] K. Koshelev, S. Kruk, E. Melik-Gaykazyan, J.-H. Choi, A. Bogdanov, H.-G. Park, and Y. Kivshar, Subwavelength dielectric resonators for nonlinear nanophotonics, *Science* **367**, 288 (2020).
- [56] V. A. Zakharov and A. N. Poddubny, Transverse magneto-optical Kerr effect enhanced at the bound states in the continuum, *Phys. Rev. A* **101**, 043848 (2020).
- [57] Z. Liu, Y. Xu, Y. Lin, J. Xiang, T. Feng, Q. Cao, J. Li, S. Lan, and J. Liu, High- $Q$  quasibound states in the continuum for nonlinear metasurfaces, *Phys. Rev. Lett.* **123**, 253901 (2019).
- [58] S. D. Krasikov, A. A. Bogdanov, and I. V. Iorsh, Nonlinear bound states in the continuum of a one-dimensional photonic crystal slab, *Phys. Rev. B* **97**, 224309 (2018).
- [59] T. Wang, Z. Li, and X. Zhang, Improved third-order nonlinear effect in graphene based on bound states in the continuum, *Photon. Res.* **5**, 629 (2017).
- [60] H. Friedrich and D. Wintgen, Interfering resonances and bound states in the continuum, *Phys. Rev. A* **32**, 3231 (1985).
- [61] F.-M. Dittes, The decay of quantum systems with a small number of open channels, *Phys. Rep.* **339**, 215 (2000).
- [62] M.-A. Miri and A. Alu, Exceptional points in optics and photonics, *Science* **363**, eaar7709 (2019).
- [63] P. Peng, W. Cao, C. Shen, W. Qu, J. Wen, L. Jiang, and Y. Xiao, Anti-parity-time symmetry with flying atoms, *Nat. Phys.* **12**, 1139 (2016).
- [64] Y. Jiang, Y. Mei, Y. Zuo, Y. Zhai, J. Li, J. Wen, and S. Du, Anti-parity-time symmetric optical four-wave mixing in cold atoms, *Phys. Rev. Lett.* **123**, 193604 (2019).
- [65] Y. Choi, C. Hahn, J. W. Yoon, and S. H. Song, Observation of an anti-PT-symmetric exceptional point and energy-difference conserving dynamics in electrical circuit resonators, *Nat. Commun.* **9**, 2182 (2018).
- [66] Y. Yang, Y.-P. Wang, J. W. Rao, Y. S. Gui, B. M. Yao, W. Lu, and C.-M. Hu, Unconventional singularity in anti-parity-time symmetric cavity magnonics, *Phys. Rev. Lett.* **125**, 147202 (2020).
- [67] Y. Li, Y.-G. Peng, L. Han, M.-A. Miri, W. Li, M. Xiao, X.-F. Zhu, J. Zhao, A. Alù, S. Fan, and C.-W. Qiu, Anti-parity-time symmetry in diffusive systems, *Science* **364**, 170 (2019).
- [68] F. Lei, J. M. Ward, P. Romagnoli, and S. Nic Chormaic, Polarization-controlled cavity input-output relations, *Phys. Rev. Lett.* **124**, 103902 (2020).
- [69] C. Li, D. Liu, and D. Dai, Multimode silicon photonics, *Nanophotonics* **8**, 227 (2019).
- [70] X. Ji, J. K. Jang, U. D. Dave, M. Corato-Zanarella, C. Joshi, A. L. Gaeta, and M. Lipson, Exploiting ultralow loss multimode waveguides for broadband frequency combs, *Laser Photonics Rev.* **15**, 2000353 (2021).
- [71] L. Zhang, S. Hong, Y. Wang, H. Yan, Y. Xie, T. Chen, M. Zhang, Z. Yu, Y. Shi, L. Liu, and D. Dai, Ultralow-loss silicon photonics beyond the singlemode regime, *Laser Photonics Rev.* **16**, 2100292 (2022).
- [72] C. Gardiner, P. Zoller, and P. Zoller, *Quantum noise: a handbook of Markovian and non-Markovian quantum stochastic methods with applications to quantum optics* (Springer Science & Business Media, 2004).
- [73] Y.-F. Xiao, M. Li, Y.-C. Liu, Y. Li, X. Sun, and Q. Gong, Asymmetric Fano resonance analysis in indirectly coupled microresonators, *Phys. Rev. A* **82**, 065804 (2010).
- [74] Z. Ye, K. Twayana, P. A. Andrekson, and V. Torres-Company, High- $Q$   $\text{Si}_3\text{N}_4$  microresonators based on a subtractive processing for Kerr nonlinear optics, *Opt. Express* **27**, 35719 (2019).
- [75] K. Twayana, Z. Ye, Ó. B. Helgason, K. Vijayan, M. K. and V. Torres-Company, Frequency-comb-calibrated swept-wavelength interferometry, *Opt. Express* **29**, 24363 (2021).
- [76] Y. Zhang, M. Menotti, K. Tan, V. Vaidya, D. Mahler, L. Helt, L. Zatti, M. Liscidini, B. Morrison, and Z. Vernon, Squeezed light from a nanophotonic molecule, *Nat. Commun.* **12**, 2233 (2021).
- [77] Y. Zhao, Y. Okawachi, J. K. Jang, X. Ji, M. Lipson, and A. L. Gaeta, Near-degenerate quadrature-squeezed vacuum generation on a silicon-nitride chip, *Phys. Rev. Lett.* **124**, 193601 (2020).
- [78] Z. Yang, M. Jahanbozorgi, D. Jeong, S. Sun, O. Pfister, H. Lee, and X. Yi, A squeezed quantum microcomb on a chip, *Nat. Commun.* **12**, 4781 (2021).
- [79] F. A. Sabattoli, H. El Dirani, L. Youssef, F. Garrisi, D. Grassani, L. Zatti, C. Petit-Etienne, E. Pargon, J. E. Sipe, M. Liscidini, C. Sciancalepore, D. Bajoni, and M. Galli, Suppression of parasitic nonlinear processes in spontaneous four-wave mixing with linearly uncoupled resonators, *Phys. Rev. Lett.* **127**, 033901 (2021).

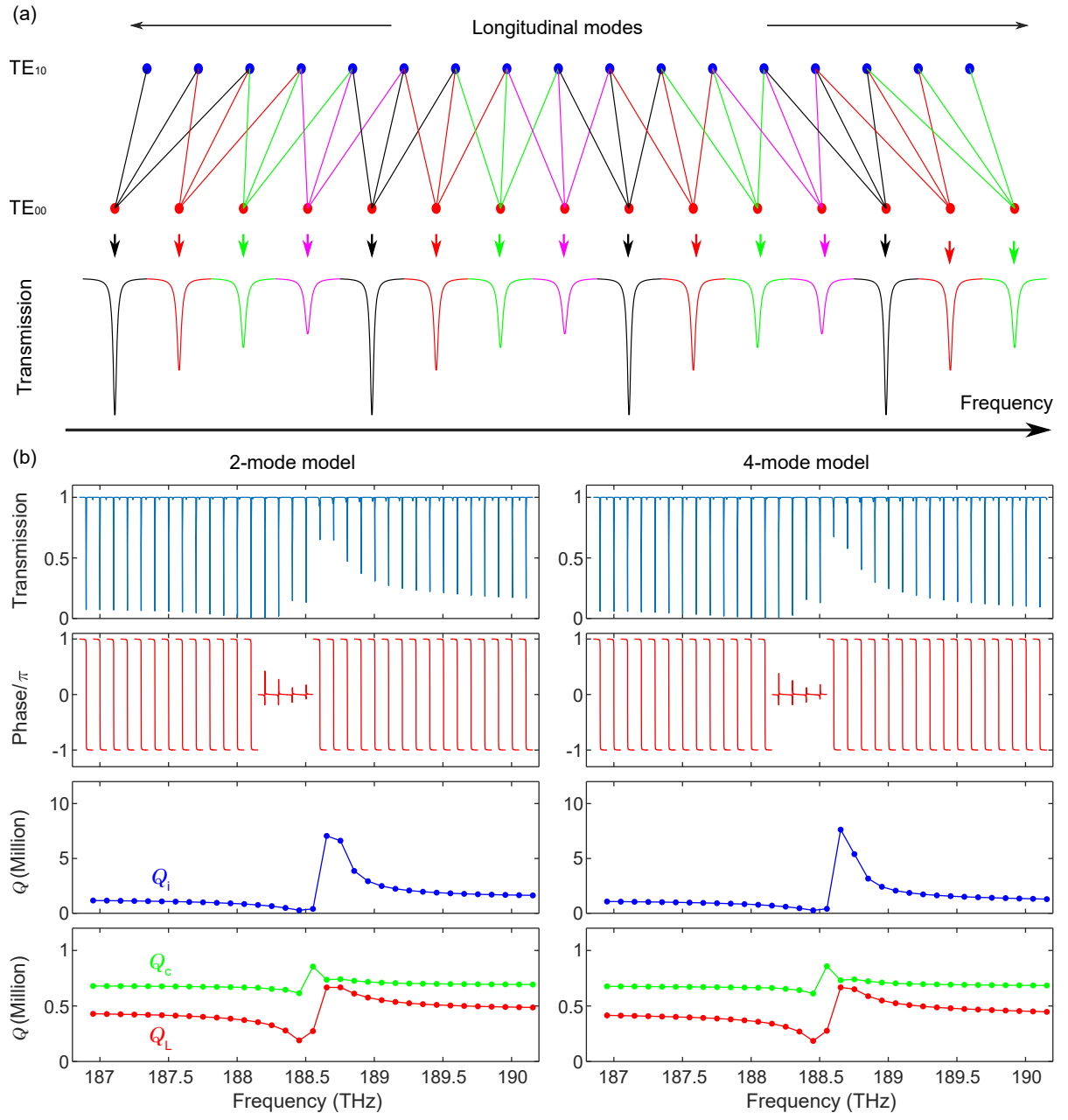


FIG. 5. Illustration of theoretical model. (a) Schematic of mode interaction in four-mode model. (b) Comparison of two-mode model and four-mode model.

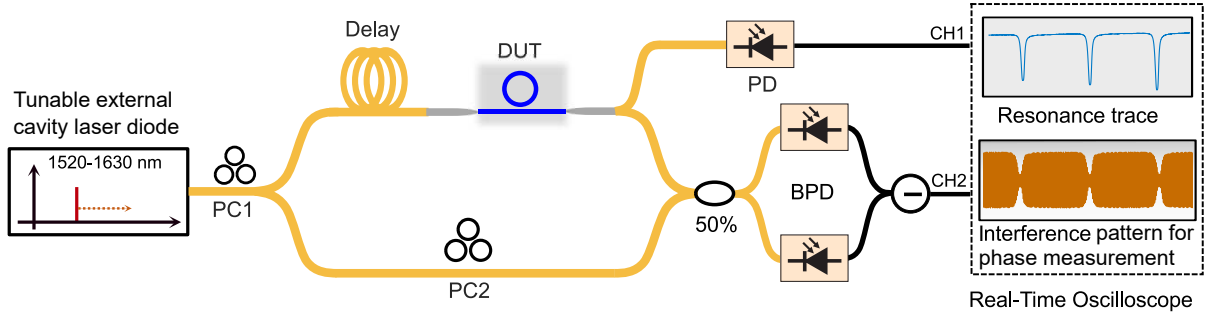


FIG. 6. Setup for spectral characterization of microresonator-waveguide systems. PC: polarization controller; PD: photodiode; BPD: balanced photodiode.

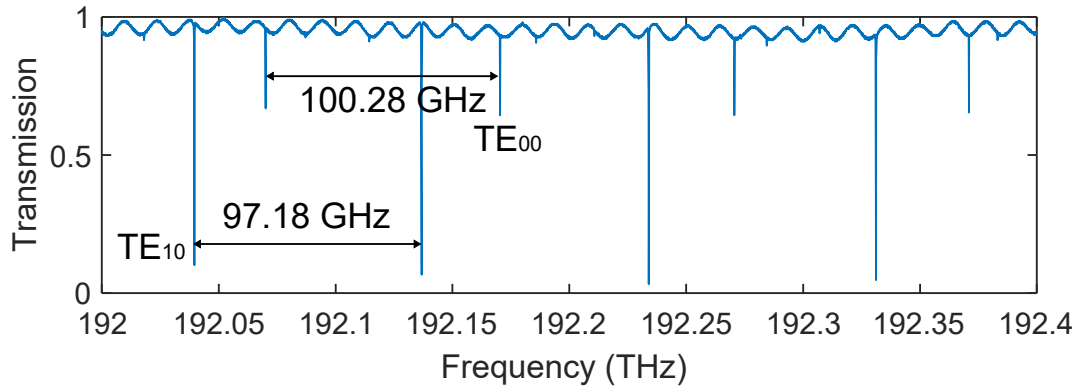


FIG. 7. Measured transmission spectrum of a microring resonator coupled with a bus waveguide. The geometry of the microring is same as the one used for Fig. 3. The width of bus waveguide is 1200 nm and the bus-ring gap is 600 nm. The input polarization aligned to the TE modes.

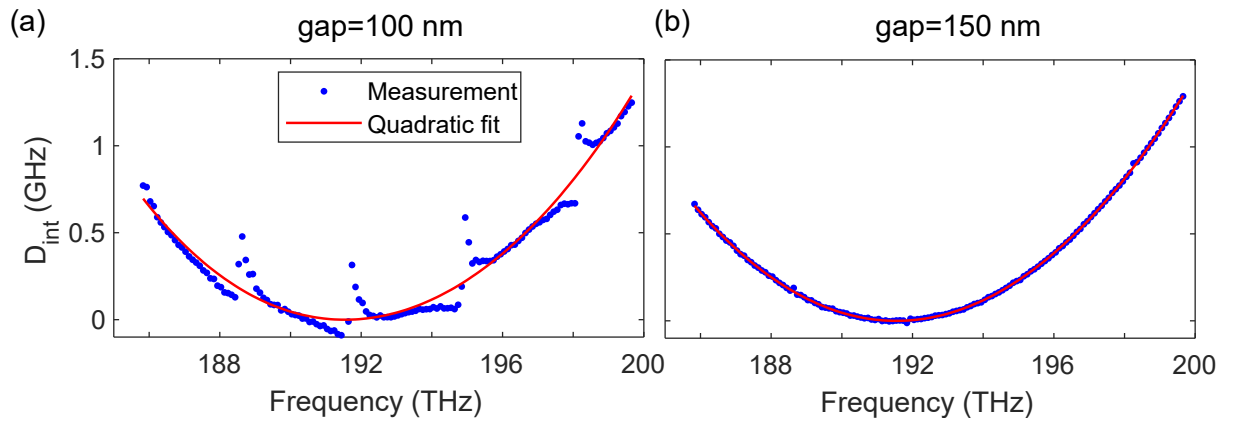


FIG. 8. Dispersion measurement. (a) Sample used for Fig. 3 in the main text. (b) Same size as (a) except for the microring-waveguide gap.

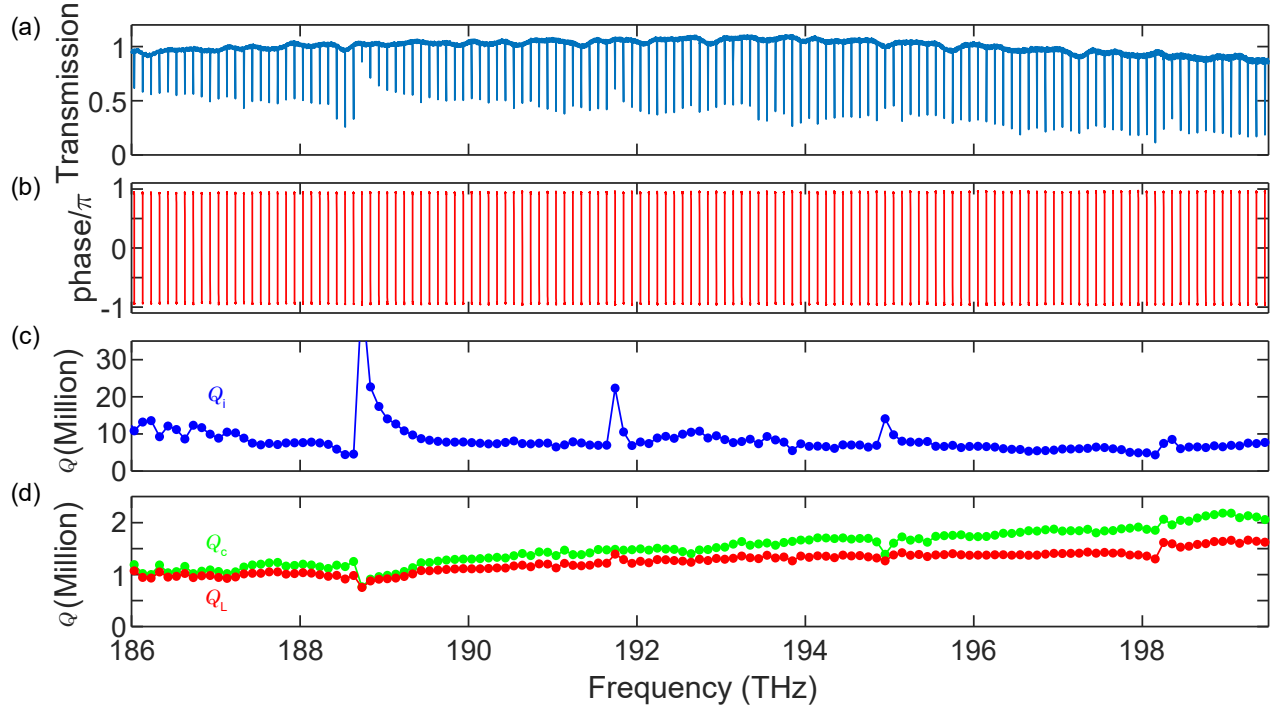


FIG. 9. Spectral characterization of the sample used for Fig. 4(c)-(d) in the main text. (a) Measured transmission spectrum (b) Phase response (c) Intrinsic  $Q_i$  (d) Coupling  $Q_c$  and loaded  $Q_L$  quality factors.

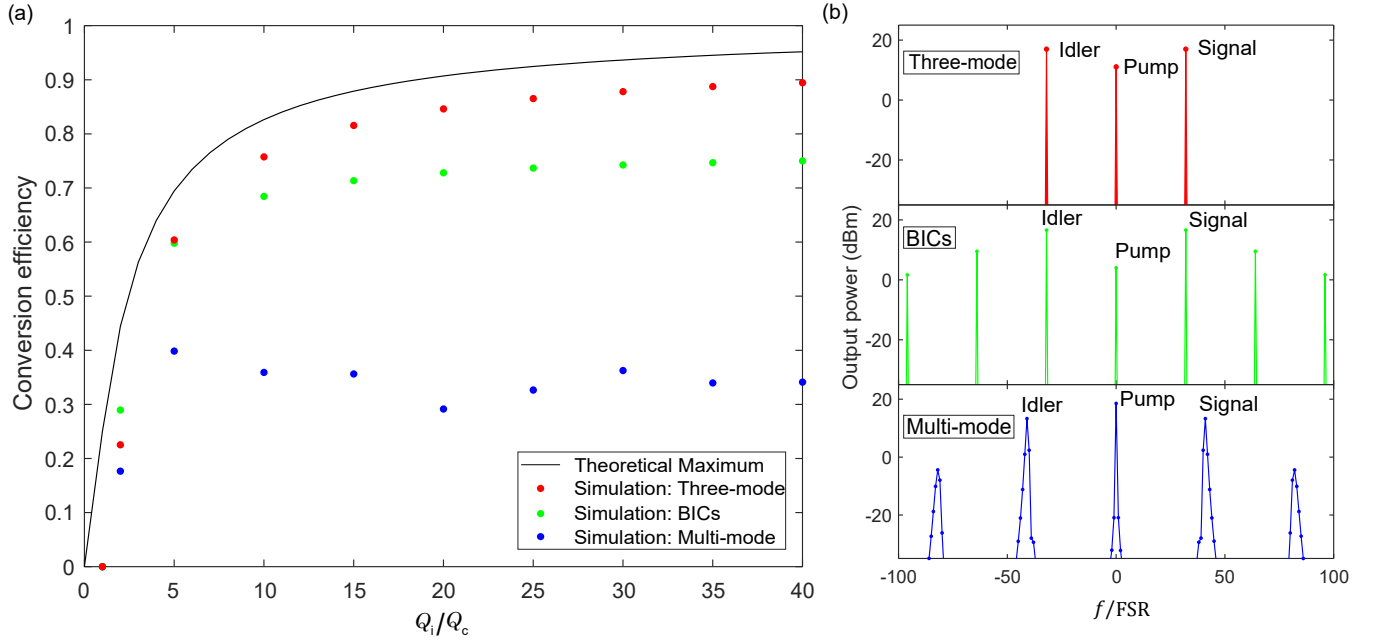


FIG. 10. Numerical simulation of conversion efficiency of h-OPO. (a) Simulated conversion efficiency as a function of quality factors. (b) Typical optical spectra corresponding to high conversion efficiency in three models.